BUTTERWORTH HEINEMANN

Mathematical model of bubble sloshing dynamics for cryogenic liquid helium in orbital spacecraft dewar container

R. J. Hung and H. L. Pan

Department of Mechanical and Aerospace Engineering, The University of Alabama in Huntsville, Huntsville, AL, USA

A generalized mathematical model is investigated of sloshing dynamics for dewar containers, partially filled with a liquid of cryogenic superfluid helium II, driven by both gravity gradient and jitter accelerations applicable to two types of scientific spacecrafts, which are eligible to carry out spinning motion and/or slew motion to perform scientific observations during normal spacecraft operation. Two examples are given for the Gravity Probe-B (GP-B) with spinning motion, and the Advanced X-Ray Astrophysics Facility-Spectroscopy (AXAF-S) with slew motion, which are responsible for the sloshing dynamics. Explicit mathematical expressions for the modelling of sloshing dynamics to cover these forces acting on the spacecraft fluid systems are derived. The numerical computation of sloshing dynamics will be based on the noninertial frame spacecraft bound coordinate, and we will solve the time-dependent three-dimensional formulations of partial differential equations subject to initial and boundary conditions. Explicit mathematical expressions of boundary conditions to cover capillary force effects on the liquid–vapor interface in microgravity environments are also derived. Results of the simulations of the mathematical model are illustrated.

Keywords: cryogenic helium, slosh dynamics, microgravity liquid-vapor interface, capillary effect

1. Introduction

In order to carry out scientific experiments, some experimental spacecraft use cryogenic cooling for observation instrumentation and telescopes and superconducting sensors for gyro read out. They also maintain very low temperatures, near absolute zero, for mechanical stability. The approaches to both cooling and control involve the use of superfluid liquid helium II. In this study, mathematical models of sloshing dynamics associated with spinning and/or slew motions are investigated. To cover the spacecraft spinning and/or slew motions, the Gravity Probe-B (GP-B) (*Figure 1*) and the Advanced X-Ray Astrophysics Facility-Spectroscopy (AXAF-S) (*Figure 2*) spacecrafts have been chosen as examples in this study. Both the GP-B and the AXAF-S spacecrafts adopt the cooling and boil-off from a cryogenic liquid helium dewar as a cryogen and propellant to maintain the cooling of instrumentations, attitude control, and drag-free operation of the spacecraft. The potential problems for cryogenic liquid in the dewar container could be due to asymmetry in the static liquid helium distribution and to perturbations in the liquid–vapor interface caused by slosh wave excitation driven by pointing control, machinery vibration, etc.

For the cases of both the GP-B and the AXAF-S spacecrafts, cryogenic liquid helium II, at a temperature of 1.3°K, is used as the propellant. Due to its superfluid behavior, there is no temperature gradient in the liquid helium. In the absence of temperature gradients along the surface, which drive Marangoni convection, the equilibrium shape of the free surface is governed by a balance of capillary, centrifugal, and gravitational forces. Determination of liquid–vapor interface profiles based on computational experiments can uncover details of the flow that cannot be visualized easily or measured experimentally in a microgravity environment.

Instabilities of the liquid–vapor interface can be induced by the presence of longitudinal and lateral accelerations. Slosh waves are thus excited that produce high and low frequency oscillations in the liquid propellant. A recent study[1] suggests that the high frequency accelerations may be unimportant in comparison with the residual motions caused by low frequency accelerations.

Time-dependent dynamical behavior of partially filled rotating dewars in reduced gravity environments was simulated by numerically solving the Navier–Stokes equations subject to initial and boundary conditions.[2–5] At the interface between the liquid and the gas, both the kinematic boundary condition and the conditions for

Address reprint requests to Dr. R. J. Hung at the Department of Mechanical and Aerospace Engineering, The University of Alabama at Huntsville, Huntsville, AL 35899, USA.

Received January 4 1994; revised February 24 1995; accepted 1 March 1995

655 Avenue of the Americas, New York, NY 10010

0307-904X/95/$10.00
SSDI 0307-904X(95)00033-G

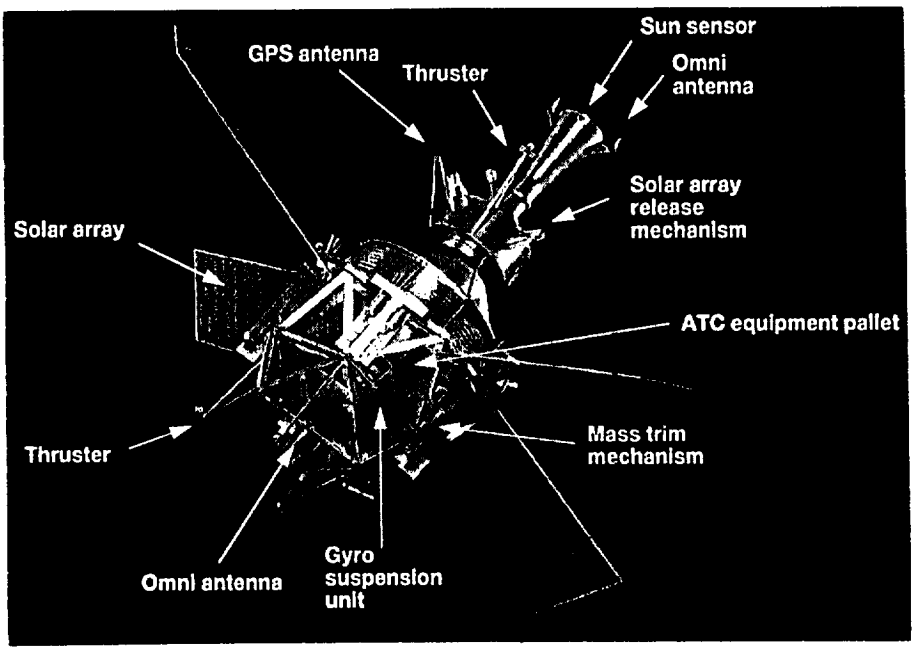

Figure 1. Gravity Probe-B (GP-B) spacecraft on-orbit configuration.

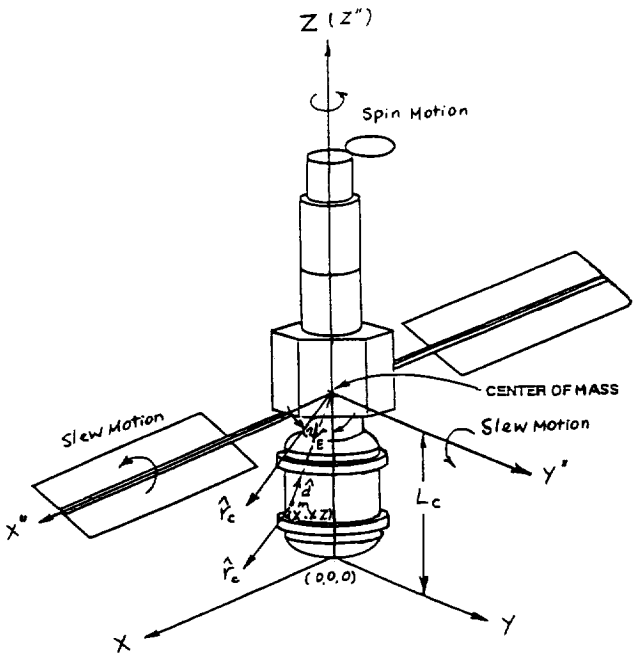

Figure 2. AXAF-S spacecraft coordinate systems with azimuth angle ψ_E from the spacecraft mass center to the center of the Earth. Coordinate (x'', y'', z'') for slew motion and coordinate (x, y, z) for fluid mechanics computations.

tangential and normal stresses at the interface were applied.[6–10] The initial conditions were adopted from the steady-state formulations developed by Hung et al.[11–14] Some of the steady-state formulations of interface shapes were compared with available experiments carried out by Leslie[15] in a free-falling aircraft (KC-135). The experiments carried out by Mason et al.[16] showed that classical fluid mechanics theory is applicable for cryogenic liquid helium in large containers.

In the spacecraft orbit around the Earth, the direction of the azimuthal angle of the Earth toward the location of the spacecraft mass center varies from 0° along the rolling axis of the spacecraft to various directions; therefore three-dimensional calculations are a must.

As the spacecraft moves along the orbit, any fluid capable of motion relative to the spacecraft is subject to the acceleration that arises from the gravity gradients of the Earth.[17–19] The interaction between the mass of fluid and the spacecraft mass due to gravity gradient accelerations[18] is capable of exciting slosh waves and disturbing the fluid system, thus inducing fluctuations in the viscous stresses and their moments with a related effect on the containers of the spacecraft. Furthermore, sources of residual acceleration of gravity jitter, including atmospheric drag on the spacecraft, background gravity, spacecraft attitude motions arising from machinery vibrations, spacecraft slew motion, thruster firings, crew motion, etc., are also capable of exciting slosh waves in the fluid containers.

Considering the dynamical behavior of helium II in a large rotating cylinder, a mixture of the superfluid and the normal fluid without separation of the two fluids is accounted for in the model computation.[20,21] The density concentration of superfluid is a function of temperature, which is also true for the surface tension and viscous coefficient for helium II.[22,23] In this study, the theory of viscous Newtonian fluids is employed with modification of transport coefficients adjusted to account for normal and superfluid density concentrations which are functions of temperature.[22,24–26]

2. Functions of scientific observations and spacecraft motions

Both the GP-B and the AXAF-S spacecrafts are sun-synchronous Earth satellites orbiting at 650 km altitude directly over the poles. The functions of scientific observation for both the GP-B and the AXAF-S spacecrafts and their motions are as follows.

2.1 The GP-B spacecraft

The GP-B spacecraft (*Figure 1*) is a relativity gyroscope experiment to test two extraordinary, universified predictions of Albert Einstein's general theory of relativity.[27,28] By using gyroscopes (those with electrically supported spheres, spinning in a vacuum, and others that utilize the spins of atomic nuclei, circulating sound waves, and even circulating laser beams), the GP-B measures two distinct space-time processes, frame dragging and the geodesic effect, which gradually change its directions of spin. In these gyroscopes, the underlying principle is that rotating systems, free from disturbing forces, should remain pointing in the same direction in space.

To comprise these functions of scientific observation, the GP-B stores its gyroscopes, telescope, probe mass, and other equipment in the center core of the dewar probe surrounded by cryogenic helium II liquid. The dewar container of the GP-B is spinning with a rotation rate of 0.1 rpm during normal operation. Because the telescope is constantly oriented on Rigel, gyro spin directions also point toward Rigel during the spacecraft motion around the polar orbit. There is no slew motion involved in the GP-B with its rotation.

2.2 The AXAF-S spacecraft

The AXAF-S spacecraft (*Figure 2*) and its sister spacecraft AXAF-I (I for imaging) are two spacecrafts restructured from the original AXAF design to carry out astrophysical observations. Equipped with the (microcalorimeter) X-Ray Spectrometer (XRS), the AXAF-S provides high throughput, high resolution, nondispersive spectroscopy at the high AXAF X-ray energies—including the astrophysically important iron-K spectral region (above 6.4 keV)—and also permits some spatially resolved high resolution spectroscopy. AXAF-S comprises a foil mirror (or possibly, a replication optic) telescope (4.7 m focal length), with XRS in the focal plane. With the baseline optical system, the AXAF-S provides important, unique capabilities for high throughput, high resolution (above 1 keV) spectroscopy of extended and point sources, and for some spatially resolved high resolution spectroscopy.

Because of the unique capabilities for high resolution spectroscopy of point and extended sources, AXAF-S is eligible to carry out the observations of distance scale stars, active galactic nuclei, clusters of galaxies, supernova remnants, X-ray binaries, etc. In this study, spacecraft slew motion without spinning with a rotating axis is required for the AXAF-S to perform its scientific mission.

3. Basic characteristics of gravity gradient and gravity jitter accelerations

Any fluid element inside the on-orbit spacecraft fluid system is subject to the acceleration that arises from the gravity gradient of the Earth.[17–19,29–33] Once the spacecraft orbit is fixed, the orbit period is determined and the basic structure of the gravity gradient acceleration can also be calculated. However, the gravity gradient acceleration acting on each fluid element inside an on-orbit spacecraft fluid system is different since it depends upon the distance of the location of the fluid element to the mass center of the spacecraft and its direction toward the location of the center of the Earth. This acceleration can only be calculated based on a noninertial frame of spacecraft-bound coordinates. Thus, the coordinate system shall be transformed from ordinary inertial frame coordinates to noninertial coordinates.

3.1 Orbit motion of spacecraft

Let us consider the cases of the GP-B and the AXAF-S spacecrafts, which are the Earth satellites orbiting at 650 km altitude directly over the poles. The orbit period, τ_o can be computed from the following expression:

$$\tau_o = 2\pi \frac{R_c^{3/2}}{R_E g_o^{1/2}} \tag{1}$$

where R_E denotes the radius of the Earth (6373 km), R_c is the radius of the circular orbit ($= R_E + h = 7023$ km), h is the orbit altitude (650 km), and g_o is Earth's gravity acceleration (9.81 m/s^2). For the case of both GP-B and AXAF-S spacecrafts, the orbit period is $\tau_o =$ 97.6 minutes and the orbit rate is $n = 2\pi/\tau_o = 1.07 \times 10^{-3}$ rad/s.

As the spacecraft is orbiting around the Earth, the azimuthal angle of the Earth, ψ_E toward the location of the spacecraft mass center varies with respect to time. At time $t = 0$, the rolling axis of the spacecraft is aligned with the radial direction of the Earth's center to the spacecraft mass center. It is assumed that the spacecraft rolling axis is linearly turning from 0° to 360° in the orbit period, τ_o, when the spacecraft is orbiting around the Earth. This is particularly true for the case of the GP-B spacecraft. Without the spacecraft slew motion, the azimuth angle (ψ_{E_o}) can be defined as

$$\psi_{E_o} = \frac{2\pi}{\tau_o} t \tag{2}$$

where t is the time measured from the instant when the direction of the spacecraft rolling axis is aligned with the radial direction of the spacecraft mass center to the center of the Earth.

3.2 Slew motion of spacecraft

In order to carry out wide-range observations, some scientific spacecrafts require slew motion with respect to their mass centers. This is particularly true for the case of the AXAF-S spacecraft. For the case of the spacecraft

slew motion, the azimuthal angle, shown in equation (2), shall be modified through the coordinate transformation of slew motion when the spacecraft is orbiting around the Earth.

Let us assume that the slew motion starts with the center located at the mass center of the spacecraft. Let us choose cartesian coordinates (x'', y'', z'') with the z''-axis along the axis of the dewar container (*Figure 1*). At time $t = 0$, the radial vector $\hat{r}_c$ from the center of the spacecraft to the center of the Earth lies on the x''–z'' plane of the cartesian coordinate chosen (*Figure 2*). The azimuth angle ψ_E is defined as the angle between the radial vector $\hat{r}_c$ and the z''-axis. The rotation matrices for spinning and/or slew motions along the x''-, y''-, and z''-axes can be expressed as

$$\begin{bmatrix} 1 & 0 & 0 \\ 0 & \cos\omega_x t & \sin\omega_x t \\ 0 & -\sin\omega_x t & \cos\omega_x \end{bmatrix}, \begin{bmatrix} \cos\omega_y t & 0 & -\sin\omega_y t \\ 0 & 1 & 0 \\ \sin\omega_y t & 0 & \cos\omega_y t \end{bmatrix}, \begin{bmatrix} \cos\omega_z t & \sin\omega_z t & 0 \\ -\sin\omega_z t & \cos\omega_z & 0 \\ 0 & 0 & 1 \end{bmatrix}$$

respectively. Here, ω_x, ω_y, and ω_z denote angular velocity of slew and/or spinning motions along the x''-, y''-, and z''-axes, respectively. The radial vector $\hat{r}_c$ in cartesian coordinates without slew and spinning motion is (*Figure 2*)

$$f_{co} = [\sin\psi_{E_o}, 0, -\cos\psi_{E_o}] \tag{3}$$

For spinning motion along the z''-axis, slew motion along the y''-axis, and slew motion along the x''-axis, the radial vector $\hat{r}_c$ is

$$\hat{r}_{c-z,y,x} = \begin{bmatrix} 1 & 0 & 1 \\ 0 & \cos\omega_x t & \sin\omega_x t \\ 0 & -\sin\omega_x t & \cos\omega_x t \end{bmatrix} \begin{bmatrix} \cos\omega_y t & 0 & -\sin\omega_y t \\ 0 & 1 & 0 \\ \sin\omega_y t & 0 & \cos\omega_y t \end{bmatrix} \begin{bmatrix} \cos\omega_z t & \sin\omega_z t & 0 \\ -\sin\omega_z t & \cos\omega_z & 0 \\ 0 & 0 & 1 \end{bmatrix} \begin{bmatrix} \sin\psi_{E_o} \\ 0 \\ -\cos\psi_{E_o} \end{bmatrix} \tag{4}$$

Mathematical formulations for the dynamics of spacecraft slew motion derived are quite general. In order to show a specific example in numerical simulation, spacecraft slew motion that operates at 90° in 600 s along the y''-axis is considered in this study.

In addition to the modification of the azimuthal angle introduced by the spacecraft slew motion through the formulation of coordinate transformation shown in equations (3) and (4), accelerations are also induced on the fluid mass in the dewar container. Accelerations acting on the fluid particle in the dewar induced by the slew motion of the spacecraft with the coordinates fixed at the spacecraft center of the mass is as follows (*Figure 2*):

$$\ddot{\mathbf{R}}_p = \boldsymbol{\omega} x(\boldsymbol{\omega} x \mathbf{R}_p) + \boldsymbol{\alpha} x \mathbf{R}_p + 2\boldsymbol{\omega} x \mathbf{v} \tag{5}$$

where $\ddot{\mathbf{R}}_p$ denotes the acceleraton vector of the fluid particle in the dewar container relative the body frame of the spacecraft, $\boldsymbol{\omega}$ is the angular velocity of the spacecraft body frame; $\boldsymbol{\alpha}$ is the angular acceleration of the spacecraft body frame, and $\mathbf{v}$ is the velocity of the fluid particle relative to the spacecraft body frame. The first, second, and third terms in the right-hand side of equation (5) denote centrifugal, angular acceleration, and Coriolis accelerations, respectively.

As indicated earlier, let us assume that the slew motion starts with the center located at the spacecraft mass center. Cartesian coordinates (x'', y'', z'') are chosen with the origin located at the spacecraft mass center. Let us also assume that the x''–z'' plane intersects the center of the Earth and the spacecraft mass center. In other words, the azimuthal angle of the Earth toward the spacecraft mass center lies in the x''–z'' plane. Slew motion is along both the x''- and y''-coordinates. Thus, $\omega_s = (\omega_{sx}, \omega_{sy}, 0)$ and $\boldsymbol{\alpha}_s = (\alpha_{sx}, \alpha_{sy}, 0)$, $\mathbf{R}_p$ due to slew motion becomes

$$\ddot{\mathbf{R}}_{p,\text{slew}} = \begin{bmatrix} \ddot{R}_{x''} \\ \ddot{R}_{y''} \\ \ddot{R}_{z''} \end{bmatrix}_{\text{slew}} = \begin{bmatrix} \omega_{sy}(\omega_{sx}R_y - R_x\omega_{sy}) + \alpha_{sy}R_z + 2\omega_{sy}v_z \\ -\omega_{sx}(\omega_{sx}R_y - R_x\omega_{sy}) - \alpha_{sx}R_z - 2\omega_{sx}v_z \\ -R_z(\omega_{sx}^2 + \omega_{sy}^2) + (\alpha_{sx}R_y - \alpha_{sy}R_x) + 2(\omega_{sx}v_y - \omega_{sy}v_x) \end{bmatrix}_{\text{slew}} \tag{6}$$

3.3 Coupling of the accelerations due to spinning and slew motions of the spacecraft

As indicated in Section 2 of this study, in specific missions of scientific observation, the dewar container of the GP-B is spinning with a certain rotating rate without slew motion during normal operation, while the AXAF-S requires slew motion for pointing control for observation of extended sources of astronomical objects without spinning. For some particular reasons required in other spacecraft, both spinning and slew motions may be needed simultaneously. In this case, the following expression with coupling for the accelerations of spinning and slew motions of the spacecraft holds:

$$\begin{aligned}\ddot{\mathbf{R}}_{\text{p, slew and spinning}} &= \begin{bmatrix}\ddot{R}_x\\ \ddot{R}_y\\ \ddot{R}_z\end{bmatrix}_{\text{slew and spinning}}\\ &= \begin{bmatrix}\omega_{sy}(\omega_{sx}R_y - \omega_{sy}R_x) + \alpha_{sy}R_z + 2\omega_{sy}v_z\\ -\omega_{sx}(\omega_{sx}R_y - \omega_{sy}R_x) - \alpha_{sx}R_z - 2\omega_{sx}v_z\\ -R_z(\omega_{sx}^2 + \omega_{sy}^2) + (\alpha_{sx}R_y - \alpha_{sy}R_x) + 2(\omega_{sx}v_y - \omega_{sy}v_x)\end{bmatrix}_{\text{slew}}\\ &+ \begin{bmatrix}-(\omega_z R_x - \omega_{sx}R_z)\omega_z - \dot{\omega}_z R_y - 2\omega_z v_y\\ (\omega_{sy}R_z - \omega_z R_y)\omega_z + \dot{\omega}_z R_x + 2\omega_z v_x\\ (\omega_{sx}R_x + \omega_{sy}R_y)\omega_z\end{bmatrix}_{\text{spinning and coupling}}\end{aligned} \tag{7}$$

where ω_z and $\dot{\omega}_x$ denote angular velocity and angular acceleration, respectively, of the spacecraft spinning motion along the z-axis.

Using $(R_x, R_y) = (r\cos\theta, r\sin\theta)$ and $(v_x, v_y) = (u_r \cdot \cos\theta - u_\theta \sin\theta, u_r \sin\theta + u_\theta \cos\theta)$ for spinning motion only, equation (7) converted from cartesian to cylindrical coordinates becomes

$$\ddot{\mathbf{R}}_{\text{p, spinning}} = \begin{bmatrix}\ddot{R}_x\\ \ddot{R}_y\\ \ddot{R}_z\end{bmatrix}_{\text{spinning}} = \begin{bmatrix}-r\cos\theta\omega_z^2 - r\sin\theta\dot{\omega}_z - 2(u_r\sin\theta + u_\theta\cos\theta)\omega_z\\ -r\sin\theta\omega_z^2 + r\cos\theta\dot{\omega}_z + 2(u_r\cos\theta - u_\theta\sin\theta)\omega_z\\ 0\end{bmatrix}_{\text{spinning}} \tag{8}$$

and

$$\ddot{\mathbf{R}}_{\text{p, spinning}} = \begin{bmatrix}\ddot{R}_r\\ \ddot{R}_\theta\\ \ddot{R}_z\end{bmatrix}_{\text{spinning}} = \begin{bmatrix}\ddot{R}_x\cos\theta + \ddot{R}_y\sin\theta\\ -\ddot{R}_x\sin\theta + \ddot{R}_y\cos\theta\\ \ddot{R}_z\end{bmatrix}_{\text{spinning}} = \begin{bmatrix}-r\omega_z^2 - 2u_\theta\omega_z\\ r\dot{\omega}_z + 2u_r\omega_z\\ 0\end{bmatrix}_{\text{spinning}} \tag{9}$$

3.4 Gravity gradient acceleration

The gravity gradient acceleration acting on the fluid mass of spacecraft is

$$\hat{\mathbf{a}}_{gg} = -n^2[3(\hat{\mathbf{r}}_c \cdot \hat{\mathbf{d}})\hat{\mathbf{r}}_c - \hat{\mathbf{d}}] \tag{10}$$

where $\hat{\mathbf{a}}_{gg}$ denotes the gravity gradient acceleration vector, $\hat{\mathbf{d}}$ is a vector (not a unit vector) from the fluid element to the spacecraft geometric center, $\hat{\mathbf{r}}_c$ is a unit vector from the spacecraft geometric center to the center of the Earth, and n is the orbit rate (*Figure 2*).

It is assumed that the gravity gradient exerted on the geometrical center of the spacecraft orbiting around the Earth on its specified orbit is zero. In other words, all the gravity acceleration exerted on the spacecraft is nothing but the gravity gradient acceleration, which is defined in equation (10).

For the convenience of mathematical calculations, let us describe all the parameters involved in equation (10) in terms of cartesian coordinates. In order to match with the computer simulation, mathematical derivations are considered in the first quadrant. *Figure 2* illustrates the geometrical relationship of the parameters shown in equation (10).

Let us consider the fluid element of interest, m, located at (r, θ, z) in cylindrical coordinates and at (x, y, z) in cartesian coordinates. The spacecraft mass center is located at $z = L_c$. Assume that vector $\hat{\mathbf{r}}_c$ lies in the x–z plane of the cartesian coordinate system. Vector $\hat{\mathbf{d}}$ in (x, y, z) coordinate becomes

$$\hat{\mathbf{d}} = [-r\cos\theta, -r\sin\theta, -(z - L_c)] \tag{11}$$

Substituting equations (4) with $\omega_x = \omega_y = 0$ and equation (11) into equation (10), the noninertial frame expression of the gravity gradient acceleration with spinning motion in z-axis becomes

$$\begin{bmatrix} a_{gg,x} \\ a_{gg,y} \\ a_{gg,x} \end{bmatrix}_{\text{spinning in } z\text{-axis}} = -n^2 \begin{bmatrix} 3[-r\sin\psi_{E_o}\cos(\theta+\omega_x t)+(z-L_c)\cos\psi_{E_o}]\sin\psi_{E_o}\cos\omega_x t + r\cos\theta \\ -3[-r\sin\psi_{E_o}\cos(\theta+\omega_z t)+(z-L_c)\cos\psi_{E_o}]\sin\psi_{E_o}\sin\omega_x t + r\sin\theta \\ -3[-r\sin\psi_{E_o}\cos(\theta+\omega_z t)+(z-L_c)\cos\psi_{E_o}]\cos\psi_{E_o} + (z-L_c) \end{bmatrix} \tag{12}$$

Substituting equations (4) with $\omega_x = \omega_z = 0$ and equation (11) into equation (10), the noninertial frame expression of the gravity gradient acceleration with slew motion along the y-axis becomes

$$\begin{bmatrix} a_{gg,x} \\ a_{gg,y} \\ a_{gg,z} \end{bmatrix}_{\text{slew in } y\text{-axis}} = -n^2 \begin{bmatrix} 3[-r\sin\psi\cos\theta+\cos\psi(z-L_c)]\sin\psi + r\cos\theta \\ r\sin\theta \\ -3[-r\sin\psi\cos\theta+\cos\psi(z=L_c)]\cos\psi + (z-L_c) \end{bmatrix} \tag{13}$$

where $\psi_E = \psi_{E_o} + \omega_y t$.

Substituting equations (4) with $\omega_y = \omega_z = 0$ and equation (11) into equation (10), the noninertial frame expression of the gravity gradient acceleration with slew motion along the x-axis becomes

$$\begin{bmatrix} a_{gg,x} \\ a_{gg,y} \\ a_{gg,z} \end{bmatrix}_{\text{slew in } x\text{-axis}} = -n^2 \begin{bmatrix} 3A\sin\psi_{E_o} + r\cos\theta \\ 3A\cos\psi_{E_o}\sin\omega_x t + r\sin\theta \\ 3A\cos\psi_{E_o}\cos\omega_x t + (z-L_c) \end{bmatrix} \tag{14}$$

where

$$A = -r\cos\theta\sin\psi_{E_o} + \cos\psi_{E_o}[r\sin\omega_x t + \cos\omega_x t(z-L_c)]$$

Thus, the gravity gradient acceleration at (r, θ, z) can be computed from that located at (x, y, z), shown in equations (12) to (14), from the following relation:

$$\hat{a}_{gg} = \begin{bmatrix} a_{gg,r} \\ a_{gg,\theta} \\ a_{gg,z} \end{bmatrix} = \begin{bmatrix} \cos\theta & \sin\theta & 0 \\ -\sin\theta & \cos\theta & 0 \\ 0 & 0 & 1 \end{bmatrix} \begin{bmatrix} a_{gg,x} \\ a_{gg,y} \\ a_{gg,z} \end{bmatrix} \tag{15}$$

3.5 Jitter accelerations

In addition to the gravity gradient acceleration acting on the fluid element of on-orbit spacecraft fluid systems, there is another acceleration of gravity jitter that also exerts forces on fluid systems. Among all of the varieties of jitter accelerations listed, accelerations induced by slew motion of the spacecraft dominate over the forces activated on the spacecraft fluid systems. The spacecraft center of mass is located at $(x_c, y_c, z_c) = (0, 0, L_c)$.

A detailed expression of $[\ddot{R}_r, \ddot{R}_\theta, \ddot{R}_z]_{\text{slew}}$ are shown in equation (9) of this paper. By putting $[\ddot{R}_r, \ddot{R}_\theta, \ddot{R}_z]_{\text{slew}} = [F_r, F_\theta, F_z]_{\text{slew}}$, jitter acceleration can be expressed as

$$\hat{a}_{gj} = \begin{bmatrix} a_{gj,r} \\ a_{gj,\theta} \\ a_{gj,z} \end{bmatrix}_{\text{slew}} + \begin{bmatrix} a_{gj,r} \\ a_{gj,\theta} \\ a_{gj,z} \end{bmatrix}_{\text{others}} = -\begin{bmatrix} F_r \\ F_\theta \\ F_z \end{bmatrix}_{\text{slew}} - \begin{bmatrix} F_r \\ F_\theta \\ F_z \end{bmatrix}_{\text{others}} [1 + \tfrac{1}{2}\sin(2\pi f t)] \tag{16}$$

where f is the jitter frequency (Hz) imposed on the fluid systems of the spacecraft.

4. Noninertial frame mathematical formulation of fundamental equations

The dynamical behavior of fluids inside on-orbit spacecraft fluid systems are strongly affected by gravity gradient and gravity jitter accelerations. In order to accommodate the effect of gravity gradient acceleration on the on-orbit fluid motion, one has to consider a noninertial frame of the spacecraft-bound coordinate rather than an inertial frame coordinate usually adapted in ordinary fluid mechanics formulations.

Consider a closed circular cylindrical dewar of radius, a, and height, L, which is partially filled with cryogenic liquid helium, and the rest of the ullage is filled with a helium vapor. The angular velocity of rotating cylinder is ω. Density and viscosity of liquid helium and helium vapor are ρ_L, μ_L, and ρ_v, μ_v, respectively.[16,24,26] Let us use cylindrical coordinates (r, θ, z), with corresponding velocity components (u, v, w), and corresponding residual gravity acceleration, such as gravity gradient components $(a_{gg,r}, a_{gg,\theta}, a_{gg,z})$ and gravity jitter components $(a_{gj,r}, a_{gj,\theta}, a_{gj,z})$. In the derivation of the governing equations, accelerations induced by the spinning motion of the spacecraft are included in the formulation. The governing equations for noninertial frame of spacecraft-bound coordinates can be shown as follows.

4.1 Continuity equation

The continuity equation is

$$\frac{1}{r}\frac{\partial}{\partial r}(ru) + \frac{1}{r}\frac{\partial v}{\partial \theta} + \frac{\partial w}{\partial z} = 0 \tag{17}$$

4.2 Momentum equations

Radial direction:

$$\rho\left(\frac{\partial u}{\partial t}+u\frac{\partial u}{\partial r}+\frac{v}{r}\frac{\partial u}{\partial \theta}-\frac{v^2}{r}+w\frac{\partial u}{\partial z}\right)$$
$$=-\frac{\partial p}{\partial r}+2\rho\omega_z v+\rho(a_{gj,r}+a_{gg,r})+\rho r\omega_z^2$$
$$+\mu\left(\nabla^2 u-\frac{u}{r^2}-\frac{2}{r^2}\frac{\partial v}{\partial \theta}\right) \quad (18)$$

Circumferential direction:

$$\rho\left(\frac{\partial v}{\partial t}+u\frac{\partial v}{\partial r}+\frac{v}{r}\frac{\partial v}{\partial \theta}+\frac{uv}{r}+w\frac{\partial v}{\partial z}\right)$$
$$=\frac{1}{r}\frac{\partial p}{\partial \theta}-2\rho\omega_z u+\rho(a_{gj,\theta}+a_{gg,\theta})-\rho r\dot{\omega}_z$$
$$+\mu\left(\nabla^2 v-\frac{v}{r^2}+\frac{2}{r^2}\frac{\partial u}{\partial \theta}\right) \quad (19)$$

Axial direction:

$$\rho\left(\frac{\partial w}{\partial t}+u\frac{\partial w}{\partial r}+\frac{v}{r}\frac{\partial w}{\partial \theta}+w\frac{\partial w}{\partial z}\right)$$
$$=-\frac{\partial p}{\partial z}+\rho(a_{gj,z}+a_{gg,z})+\mu\nabla^2 w \quad (20)$$

where

$$\nabla^2=\frac{1}{r}\frac{\partial}{\partial r}\left(r\frac{\partial}{\partial r}\right)+\frac{1}{r^2}\frac{\partial^2}{\partial \theta^2}+\frac{\partial^2}{\partial z^2} \quad (21)$$

In these equations, $2\omega_z v$ and $2\omega_z u$ are the Coriolis acceleration, $r\omega_z^2$ is the centrifugal acceleration, and $r\dot{\omega}_z$ is the angular acceleration induced by the spinning motion of the spacecraft.

In the computation of fluid forces, moments, viscous stresses, and angular moments acting on the container wall of the spacecraft, one has to consider those forces and moments in the inertial frame rather than in the noninertial frame. To show an example, one has to transform those vectors from the noninertial frame to the inertia frame for the case of spinning motion in the z-axis.

$$\begin{bmatrix}F_x'\\F_y'\\F_z'\end{bmatrix}=\begin{bmatrix}\cos\omega_z t & -\sin\omega_z t & 0\\ \sin\omega_z t & \cos\omega_z t & 0\\ 0 & 0 & 1\end{bmatrix}\begin{bmatrix}F_x\\F_y\\F_z\end{bmatrix} \quad (22)$$

where primes denote vectors in the inertia frame while those parameters without the primes indicate vectors in the non-inertial frame.

5. Initial and boundary conditions of spacecraft fluid system in the microgravity environment

The governing equations of the fluid motion in on-orbit spacecraft fluid systems in a noninertial frame of spacecraft-bound coordinates have been illustrated in equations (17) to (22). These equations shall be combined with the characteristics of gravity gradient and gravity jitter accelerations as formulated in equations (1) to (16). Initial and boundary conditions shall be introduced to solve for the fluid motion in an on-orbit spacecraft fluid system in noninertial frame coordinates.[14,34–37]

Let the profile of the interface between gaseous and liquid fluids be given by

$$\eta(t, r, \theta, z)=0 \quad (23)$$

The initial condition of the profile of the interface between gaseous and liquid fluids at $t=t_0$ is assigned explicitly and is given by

$$\eta(t=t_0, r, \theta, z)=0 \quad (24)$$

A set of boundary conditions has to be supplied for solving the equations. The initial interface profiles used in this study have been given explicitly through the steady-state computations made by Hung and Leslie[38] and Hung and Shyu,[39,40] which were checked with the experiments carried out by Leslie.[15] These boundary conditions are as follows:

(1) Along the container wall, the following three boundary conditions apply:
   (a) Interface between solid and liquid: No penetration and no slip conditions assure that both the tangential and the normal components of the liquid velocity along the solid walls vanish.
   (b) Interface between solid and gaseous (vapor) fluid: Similar no penetration and no slip conditions as that for the interface between solid and liquid will apply.
   (c) At the location of solid–liquid–gaseous (vapor) three-phase interface: No penetration, but slip conditions apply. This will assure that normal components of liquid and vapor velocities along the solid wall vanish and allow a slipping flow of liquid and vapor fluids along the solid wall at the three-phase interface. The velocity of slipping flow at this location is governed by the adhesive forces between fluids (liquid and gas) and solid walls. Also, at the three-phase interface, a constant contact angle is present in which the behavior of wet or dry contacts are determined by molecular physics scale Coulomb interaction between the fluids (liquid and vapor) and the surface phenomena (material, polishing, and roughness) of solid walls. Mathematical computation of the interphase contact angle is very complicated, involves the molecular physics scope of microscale, and is not realistic to carry out such a computation in this sloshing dynamics modelling. In this study, experimental measurement of contact angle is employed in the mathematical modelling.

(2) Along the interface between the liquid and gaseous fluids, the following two conditions apply:

   (a) Kinematic boundary condition: The liquid (or gaseous) surface moves with the liquid (or gas)

which implies

$$\frac{D\eta}{Dt} = 0$$

$$\text{or} \quad \frac{\partial \eta}{\partial t} + u\frac{\partial \eta}{\partial r} + \frac{v}{r}\frac{\partial \eta}{\partial \theta} + w\frac{\partial \eta}{\partial z} = 0 \qquad (25)$$

$$\text{on} \quad \eta(t = t_\alpha, r, \theta, z)$$

(b) Interface stress conditions: At the liquid–vapor interface, the stress must be continuous. Based on Landu and Lifshitz, the stress across the liquid–vapor interface can be expressed as

$$(P_G - P_L)n_i - [(\tau_{ij})_G - (\tau_{ij})_L]n_j = \sigma\left(\frac{1}{R_1} + \frac{1}{R_2}\right)n_i \qquad (26)$$

where R_1 and R_2 are the radii of curvature.

The expressions of radii of curvature R_1 and R_2 in cylindrical coordinates from differential geometry are

$$\frac{1}{R_1} + \frac{1}{R_2} = -\frac{1}{r}\left[\frac{\partial}{\partial r}\left(r\frac{H_r}{D}\right) + \frac{\partial}{\partial \theta}\left(\frac{H_\theta}{rD}\right)\right] \qquad (27)$$

where

$$[H_r, H_\theta] = \left[\frac{\partial}{\partial r}, \frac{\partial}{\partial \theta}\right]H$$

and

$$D = \left(1 + H_r^2 + \frac{1}{r^2}H_\theta^2\right)^{1/2}$$

In equation (26)

$$\tau_{ij} = \mu\left(\frac{\partial u_i}{\partial x_j} + \frac{\partial u_j}{\partial x_i} + \frac{2}{3}\frac{\partial u_k}{\partial x_k}\delta_{ij}\right) + \zeta\frac{\partial u_k}{\partial x_k}\delta_{ij}$$

is the viscous stress tensor, μ is the viscous coefficient of the first kind, ζ is the viscous coefficient of the second kind, P is the pressure, σ is the surface tension of the liquid–vapor interface, n_j is the unit vector normal to the interface, δ_{ij} is the Kronecker's delta, and subscripts G and L denote conditions in the gaseous and liquids fluids, respectively, across the liquid–vapor interface.

The fluid stresses across the liquid–vapor interface can be decomposed into a normal (n_i, a unit vector) and tangential (t_i, a unit vector) components to the interface. For the tangential component to the interface, one can take a dot product of a unit vector tangential to the interface, t_i, to equation (26), which yields

$$[(\tau_{ij}t_in_j)]_L = [(\tau_{ij}t_in_j)]_G \qquad (28)$$

since $n_it_i = 0$.

For the normal component to the interface, one can also take a dot product of a unit vector normal to the interface, n_i, to equation (26), which leads to

$$P_G - P_L - [(\tau_{ij}n_in_j)_G - (\tau_{ij}n_in_j)_L] = -\frac{\sigma}{r}\left[\frac{\partial}{\partial r}\left(\frac{rH_r}{D}\right) + \frac{\partial}{\partial \theta}\left(\frac{H_\theta}{rD}\right)\right] \qquad (29)$$

6. Methods of mathematical modelling simulation

Detailed descriptions of the computational algorithm applicable to cryogenic fluid management under microgravity are also given in our earlier studies.[37,42] In this study, full-scale GP-B and AXAF spacecraft propellant dewar tanks with a radius of 68 cm and a height of 145 cm will be used in the numerical simulation (*Figure 3*). The propellant tank is 80% filled with cryogenic liquid helium and the rest of the ullage is filled with helium vapor. Temperature of the cryogenic helium is 1.3°K. In this study, the following data were used: liquid helium density = 0.145 g/cm^3, helium vapor density = 0.00147 g/cm^3, fluid pressure = 1.66×10^3 dyne/cm^2, surface tension at the interface between the liquid helium and the helium vapor = 0.346 dyne/cm, liquid helium viscosity coefficient = 1.12×10^{-4} cm^2/s (first viscosity coefficient only is considered because of the nature of incompressible flow which makes the effect of second viscosity vanishing in this case); and contact angle = 0°. The initial profiles of the liquid–vapor interface for the rotating dewar are determined from computations based on algorithms developed for the steady-state formulation of microgravity fluid management.[36,37]

A staggered grid for the velocity components is used in this computer program. The method was developed by Harlow and Welch[43] for their MAC (marker-and-cell) method for flows with a free surface. The finite difference method employed in this numerical study was the "Hybrid Scheme" developed by Spalding.[44] The formulation for this method is valid for any arbitrary interface location between the grid points and is not limited to middle point interfaces.[45] A semi-implicit method[46] was used as the procedure for modelling the flow field. The time step is determined automatically based on the size of the grid space and the velocity of

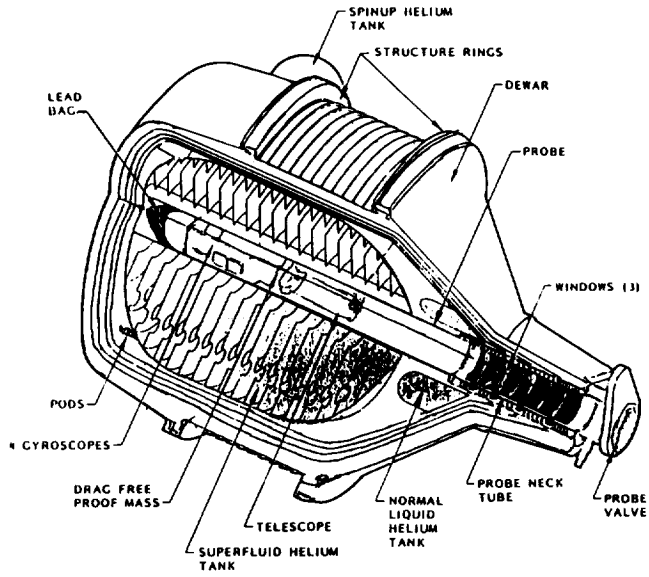

Figure 3. The GP-B module showing main elements of liquid helium dewar, probe, and baffle-boards.

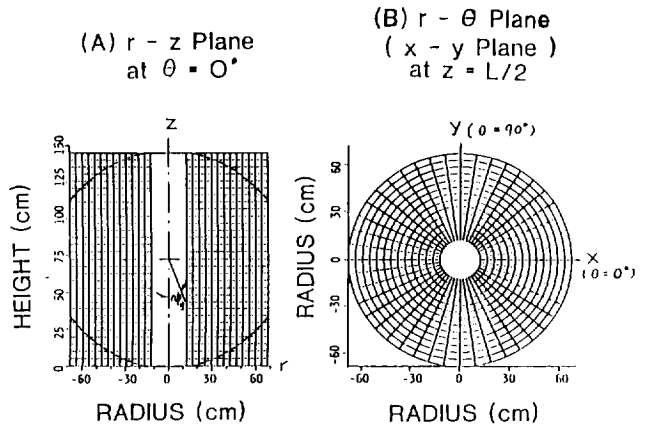

Figure 4. Distribution of grid points in the (A) radial-axial plane and (B) radial-circumferential plane of the cylindrical coordinates for the GP-B dewar tank.

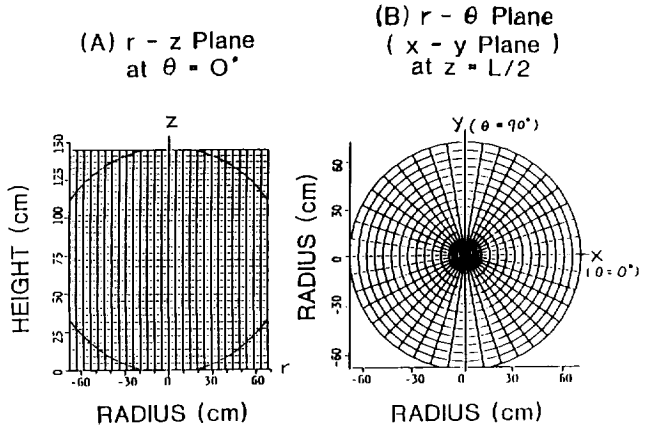

Figure 5. Distribution of grid points in the (A) radial-axial plane, and (B) radial-circumferential plane of the cylindrical coordinates for the AXAF-S dewar tank.

the flow field. A detailed description of the computational algorithm applicable to microgravity fluid management is illustrated in our earlier studies.[14] *Figures 4a* and *4b* show the distribution of grid points for the dewar tank with the probe for the GP-B dewar container in the radial-axial plane and radial-circumferential plane, respectively, in cylindrical coordinates. *Figures 5a* and *5b* show the distribution of grid points for the dewar tank for the AXAF-S spacecraft in the radial-axial plane and radial-circumferential plane, respectively, in cylindrical coordinates.

7. Spacecraft sloshing dynamics associated with spinning and/or slew motions

By using the mathematical formulations illustrated in the previous sections, one can simulate numerically the spacecraft sloshing dynamics associated with spinning and/or slew motions depending upon the specific scientific missions assigned to the spacecraft. Examples are given to illustrate the sloshing dynamics associated with spinning motion for the GP-B spacecraft and the sloshing dynamics associated with slew motion for the AXAF-S spacecraft.

7.1 Sloshing dynamics associated with spinning motion for the GP-B spacecraft

As described earlier, the dewar container of the GP-B is spinning with a rotation rate of 0.1 rpm during its normal operation. The noninertial frame equations, shown in equations (17)–(21), subject to initial and boundary conditions, shown in equations (23)–(29), shall be considered in our computation. As for gravity gradient acceleration, the noninertial frame expressions of equations (12) and (15) for spinning motion in the z-axis shall be adopted. For gravity jitter acceleration, all induced forces except forces due to slew motion shall be considered since the acceleration induced by the spinning motion has been included in the equations, shown in equations (18) and (19). Thus, gravity jitter acceleration, shown in equation (4), can be rewritten as

$$\hat{\mathbf{a}}_{gj} = \begin{bmatrix} a_{gj,r} \\ a_{gj,\theta} \\ a_{gj,z} \end{bmatrix} = g \begin{bmatrix} \sin\psi_{E_0}\cos(\theta + \omega_z t) \\ -\sin\psi_{E_0}\sin(\theta + \omega_z t) \\ \cos\psi_{E_0} \end{bmatrix} \{1 + \tfrac{1}{2}(\sin 2\pi f t)\} \quad (30)$$

Figure 6 shows the time variation of gravity gradient acceleration for a turnaround period of 1,200 s with container rotating speed (ω_z) of 0.1 rpm for the components along the (x, y, z) directions acted on the fluid mass located at (r, θ, z) = (40 cm, $\pi/4$, 10 cm). *Figure 6* shows that the magnitude of gravity gradient acceleration is on the order of $10^{-7}\, g_0$ ($g_0 = 981$ cm/s^2). *Figure 7* shows the time variation of the gravity jitter acceleration for a turn-around period of 1,200 s with a container rotating speed (ω_z) of 0.1 rpm and a jitter frequency (f) of 0.1 Hz for components along the (x, y, z) directions acted on the fluid mass everywhere in the container. Two ranges of background cavity, 10^{-6} and $10^{-8}\, g_0$ for gravity jitter accelerations that correspond to accelerations higher and lower, respectively, than that of the gravity gradient acceleration are presented.

The grid point distribution in the dewar tanks, shown in *Figure 4*, is adopted for this example of the GP-B dewar. The present study is basically a simulation of an initial value problem. An improper assignment of initial profile of bubbles for the initial conditions will result in a wrong conclusion of simulation in this study. The initial conditions of the bubble shape shall be computed from the conditions of bubble configuration with minimum Gibbs free energy which is a function of surface tension, gravitational, and centrifugal accelerations together with the liquid-fill level and geometry of the container. The equilibrium shape of the liquid–vapor interface for a rotating dewar under a residual gravity environment below $10^{-6}\, g_0$ and a rotating speed of 0.1 rpm is very much alike and is a doughnut configuration with a near circular kidney-shaped cross-section based on the computation of the numerical

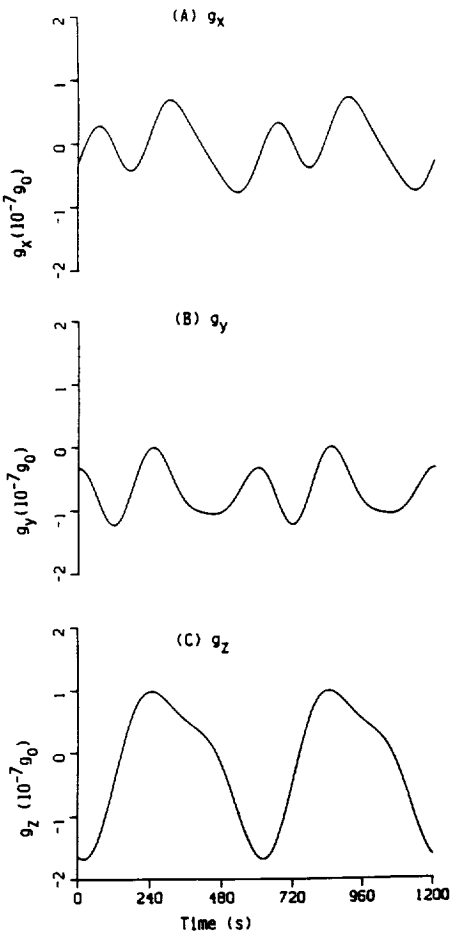

Figure 6. Time variation of GP-B spacecraft gravity gradient acceleration acting on fluid mass located at $(r, \theta, z) = (40\text{ cm}, \pi/4, 40\text{ cm})$ for a turn-around period of 1,200 s with rotating speed of 0.1 rpm, along (A) the x-direction; (B) the y-direction; (C) the z-direction. $\omega = 0.1$ rpm; $\tau = 1{,}200$ s; $g_o = 9.81\ \text{m/s}^2$.

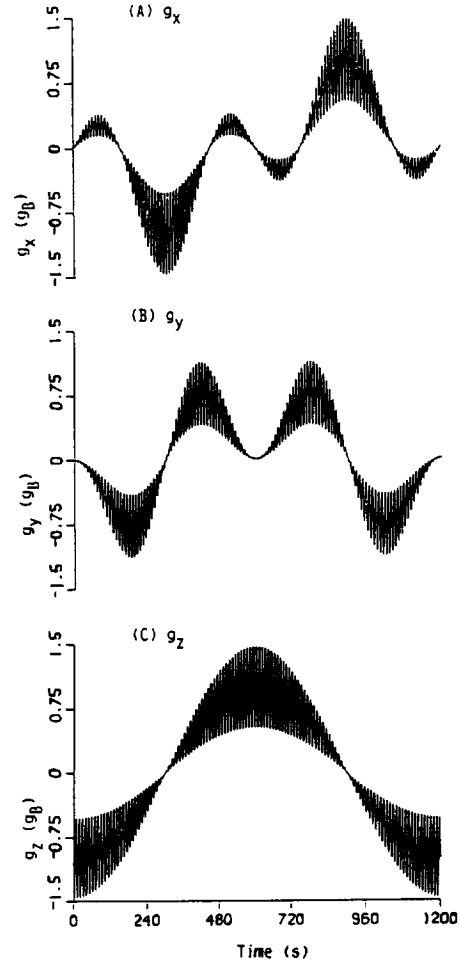

Figure 7. Time variation of GP-B spacecraft gravity gradient acceleration acting on the fluid system under background gravity of 10^{-8} and $10^{-6}\ g_o$, rotating speed of 0.1 rpm, turn- around period of 1,200 s and gravity jitter frequency of 0.1 Hz, along (A) the x-direction; (B) the y-direction; and (C) the z-direction.

algorithm developed in our earlier studies.[34,35] *Figure 8a* shows the initial profile of the liquid–vapor interface in the r–z plane at $\theta = 0°$ and 180°. *Figure 8b* shows the initial profile of the liquid–vapor interface in the r–z plane at $\theta = 90°$ and 270°. *Figure 8c* shows the initial profile of the liquid–vapor interface in the r–θ plane at a height $z = 108$ cm. *Figure 8d* shows the initial profile of the three-dimensional liquid–vapor interface. By using initial conditions of the bubble profiles described in *Figure 8*, one can proceed with the simulation of bubble sloshing dynamics activated by orbital accelerations.

The sloshing dynamics of the GP-B spacecraft driven by the combined effects of gravity gradient and a $10^{-8}\ g_o$ background jitter acceleration associated with spinning motion in the z-axis has been studied. In this case, the combined forces are dominated by the gravity gradient acceleration. *Figure 9* shows the time sequence evolution of the three-dimensional dynamical behavior of the interface oscillations driven by these combined accelerations. The figure shows the time sequence of the bubble oscillations due to the GP-B sloshing dynamics at times $t = 191$, 354, 380, 431, 503, 603, 825, 980, 995, 1,050, 1,080, and 1,200 s. It clearly shows that there are a series of asymmetric oscillations excited along the liquid–vapor interface driven by the asymmetric gravity gradient dominated acceleration associated with spinning motion along the z-axis.

With reference to equation (13), the gravity gradient acceleration exerted on the spacecraft is equivalent to the combination of time-dependent force with tidal motion and torsional moment acting on the spacecraft fluid mass when it is orbiting around the Earth.[6,7] *Figure 9* shows the simulation of time animation of how the bubble deforms in response to the time-dependent force with tidal motion and torsional moment characterized by the gravity gradient dominated accelerations activated on the rotating dewar.

Time fluctuations of the locations of bubble mass centers of the rotating container due to slosh waves excited by gravity gradient dominated acceleration based on *Figure 9* have been computed. The values of bubble mass center fluctuations are $(\Delta x_c, \Delta y_c, \Delta z_c) = (4.54,$

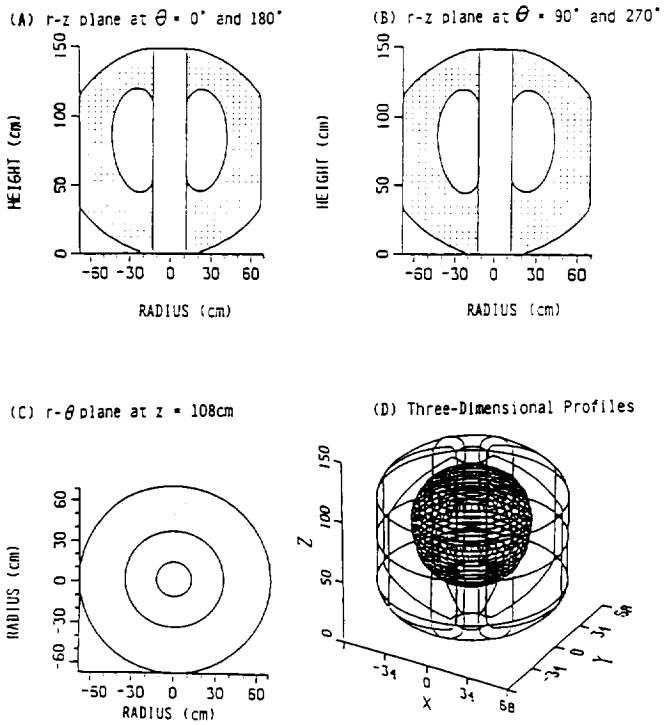

Figure 8. Initial profiles of liquid–vapor interface for the Gravity Probe-B module of a rotating dewar under background gravity of $10^{-7}\ g_o$, rotating speed of 0.1 rpm, direction of background gravity at $\psi_E = 0°$, and gravity jitter frequency of 0.1 Hz. In (A) the r–z plane at $\theta = 0°$ and 180°, (B) the r–θ plane at $\theta = 90°$ and 270°, (C) the r–θ plane at $z = 108$ cm, and (D) the three-dimensional liquid–vapor interface profile.

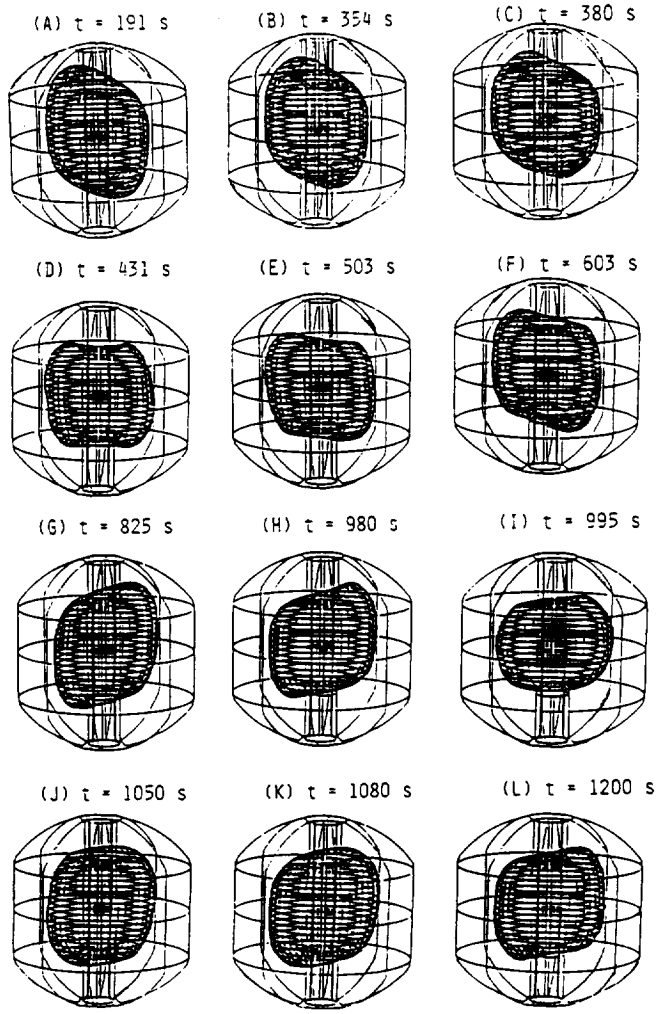

Figure 9. Time sequence evolution of the GP-B spacecraft three-dimensional liquid–vapor interface oscillations for a rotating dewar driven by combined gravity gradient and jitter accelerations with background gravity of $10^{-8}\ g_o$. The rotating speed of the dewar is 0.1 rpm, and the period of gravity direction turn-around time is 1,200 s.

2.83, 2.32) cm. It shows that $\Delta x_c > \Delta y_c > \Delta z_c$ for bubble mass center fluctuations driven by gravity gradient dominated acceleration.

The combined effects of gravity gradient and a $10^{-6}\ g_o$ background jitter acceleration associated with spinning motion have also been studied. In this case, the combined forces are dominated by the jitter acceleration. *Figure 10* shows the evolution of the three-dimensional dynamical behavior of the sloshing dynamics governed interface oscillations driven by the gravity jitter dominated acceleration of 0.1 Hz, i.e., a low jitter frequency. It clearly shows that there are a series of asymmetric oscillations excited along the surface of the liquid–vapor interface driven by asymmetric gravity jitter dominated acceleration.

With reference to equation (17), gravity jitter acceleration exerted on the spacecraft is equivalent to time-dependent oscillatory forces that push the bubble in the combined directions of down-and-up and leftward-and-rightward as the bubble is rotating with respect to the spacecraft rotating axis. *Figure 10* shows the simulation of how the bubble deforms in response to the time-dependent up-and-down and leftward-and-rightward forces characterized by the jitter dominated accelerations activated on the rotating dewar.

Time fluctuations of the locations of bubble mass centers of the rotating container due to slosh waves excited by asymmetric jitter-dominated acceleration based on *Figure 10* have been computed. The values of bubble mass center fluctuations are $(\Delta x_c, \Delta y_c, \Delta z_c) = (17.28, 12.2, 33.83)$ cm. A comparison of *Figures 9* and *10* for bubble mass center fluctuations between that driven by gravity gradient dominated and that given by jitter dominated accelerations provides the following conclusions. (a) Dynamics of bubble (liquid–vapor interface) driven by gravity gradient dominated acceleration produces bubble mass center fluctuations of $\Delta x_c > \Delta y_c > \Delta z_c$ while up and down oscillations of bubble driven by jitter dominated acceleration induces bubble mass center fluctuations of $\Delta z_c > \Delta x_c > \Delta y_c$. (b) A comparison of the values of bubble mass center fluctuations show that fluctuations of bubble mass center induced by jitter dominated acceleration is greater than that induced by gravity gradient dominated acceleration. (c) Fluctuations of both x_c and y_c start from zero while that of the z_c starts from a non-zero value at the middle

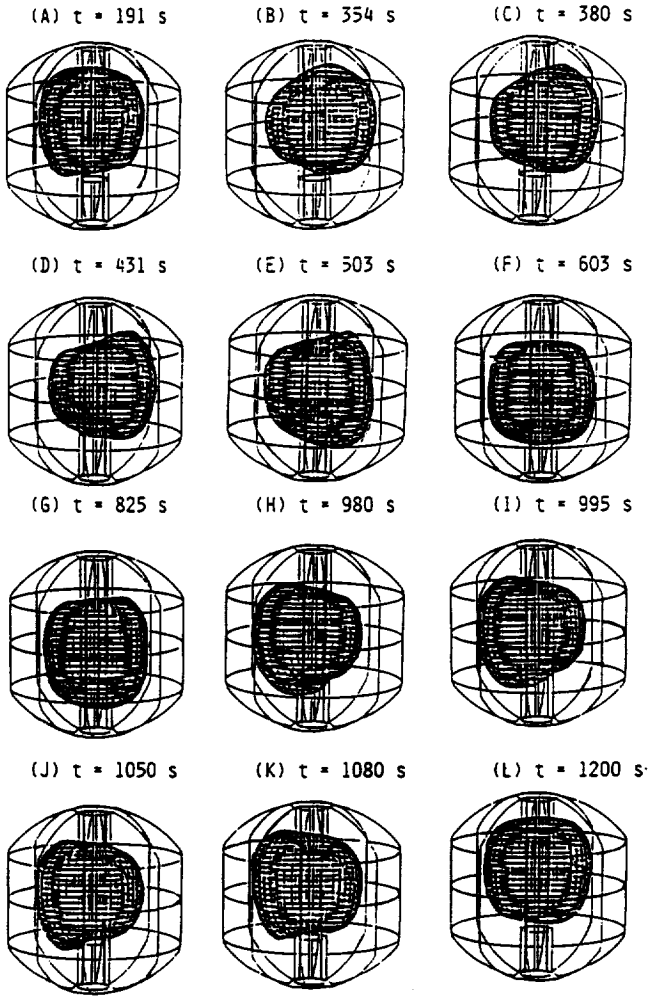

Figure 10. Time sequence evolution of the GP-B spacecraft three-dimensional liquid–vapor interface oscillations driven by combined gravity gradient and jitter accelerations of 0.1 Hz frequency, background gravity of $10^{-6}\ g_o$ with the period of gravity direction turn-around time = 1,200 s, and rotating speed of 0.1 rpm.

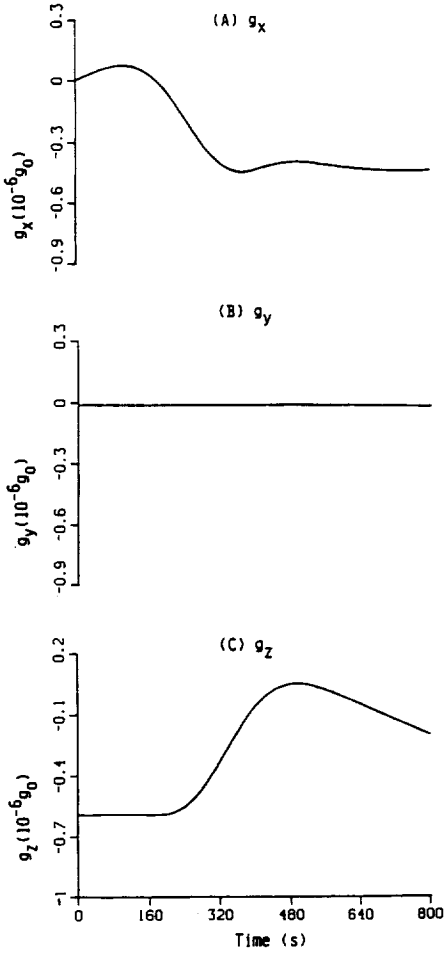

Figure 11. Time variation of AXAF-S spacecraft gravity gradient acceleration acting on fluid mass located at (r, θ, z) = (12 cm, $\pi/2$, 3 cm) for 90° slew motion in 10 minutes along the y''-axis and orbital period of 97.6 minutes along (A) the x-direction; (B) the y-direction; (C) the z-direction. $g_o = 9.81\ m/s^2$.

point of the height of partially filled liquid container. (d). Fluctuation magnitudes of x_c, y_c, and z_c associated with higher jitter frequency are lower than those of the frequencies associated with lower jitter frequency for bubble mass center fluctuations driven by jitter dominated acceleration.

7.2 Sloshing dynamics associated with slew motion for the AXAF-S spacecraft

Assuming that the slew motion is along the y''-axis (*Figure 2*), the gravity gradient acceleration associated with slew motion can be computed from the noninertial frame expressions of equations (8) and (10). It is assumed that the slew motion operates at 90° in 600 s.

In this example, the spacecraft sloshing dynamics driven by gravity gradient acceleration associated with slew motion along the y''-axis, shown in *Figure 2*, have been investigated. As the orbital period of the AXAF-S spacecraft is 97.6 minutes, and the period of slew motion along the y''-axis is 600 s. The component of gravity gradient acceleration along the (x, y, z) directions on a fluid mass located at $(r, \theta, z) = (12\ cm, \pi/2, 3\ cm)$ is shown in *Figure 11*. This figure shows that the magnitude of the gravity gradient acceleration is on the order of $10^{-7}\ g_o$ for the AXAF-S dewar on its operation orbit. The distance from the spacecraft mass center to the bottom of the dewar, L_c, shown in *Figure 2*, is 257.8 cm. The grid point distribution of the dewar tanks, shown in *Figure 5*, is adopted for the AXAF-S dewar.

As indicated earlier, the initial shape of the bubble shall be given with the consideration of surface tension and gravitational acceleration, together with the liquid fuel level and the geometry of the container based on the computation of the minimum Gibbs free energy of the bubble. The equilibrium shape of the liquid–vapor interface for a dewar with 70% liquid-filled level under a residual gravity environment below $10^{-7}\ g_o$ is a sphere. *Figure 12a* shows the initial shape of the interface in the r–z plane at $\theta = 0°$ and 180°. *Figure 12b* shows the initial

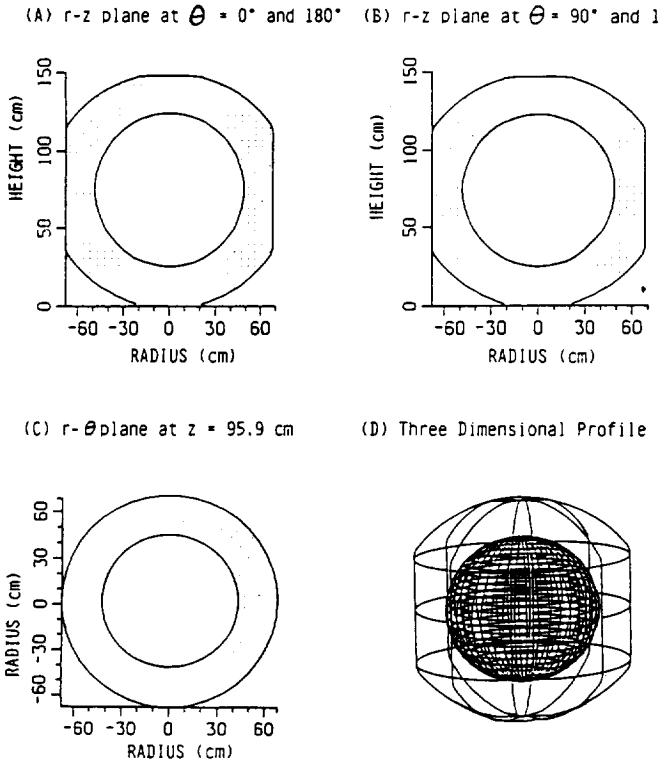

Figure 12. Initial profiles of liquid–vapor interface for AXAF-S spacecraft of dewar tank under background gravity of 10^{-7} g_o, and direction of background gravity at $\psi_E = 0°$. In (A) the r–z plane at $\theta = 0°$ and 180°, (B) the r–θ plane at $\theta = 90°$ and 270°, (C) the r–θ plane at $z = 95.9$ cm, and (D) the three-dimensional liquid–vapor interface profile.

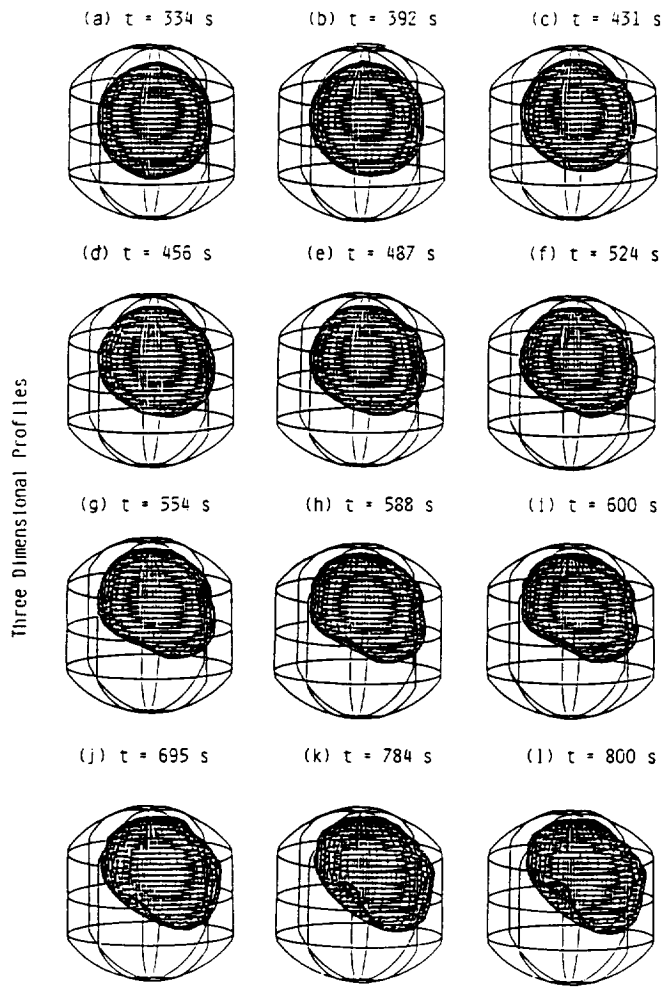

Figure 13. Time sequence evolution of the AXAF-S spacecraft three-dimensional liquid–vapor interface oscillations for a dewar driven by gravity gradient acceleration associated with slew motion in the y''-axis. An orbital period of 97.6 minutes and 90° slew motion in 10 minutes are applied to the spacecraft operation.

profile of the liquid–vapor interface in the r–z plane at $\theta = 90°$ and 270°. *Figure 12c* shows the initial profile of the liquid–vapor interface in the r–θ plane at height $z = 95.9$ cm. *Figure 12d* shows the initial profile of three-dimensional liquid–vapor interface. Time-dependent simulation can be performed based on the initial conditions with the bubble profiles specified in *Figure 12*.

The sloshing dynamics of the AXAF-S spacecraft driven by the gravity gradient acceleration associated with slew motion along the y''-axis, shown in *Figure 2*, have been investigated. *Figure 13* shows the time evolution of the three-dimensional dynamical behavior of the interface oscillations driven by gravity gradient acceleration associated with slew motion.

With reference to the characteristics of gravity gradient acceleration associated with slew motion, shown in *Figure 11*, liquid is pushed toward the negative x-direction and the negative z-direction with gradually decreasing values initially and increasing values later but still in the negative direction. This makes the bubble to be pushed toward the positive x-direction and positive z-direction with decreasing and increasing accelerations correctively. The uneven and imbalance flow velocities induced by gravity gradient acceleration associated with slew motion toward the positive x- and positive z-directions create a similar uneven and imbalanced pressure distribution on the bubble which have resulted in a deformed irregular concave- and convex-shaped oscillating bubble shown in *Figure 13*.

Time fluctuations of the locations of bubble mass centers of the fluids inside the dewar container due to sloshing dynamics driven by gravity gradient acceleration associated with slew motion based on *Figure 13* have been computed. The values of bubble mass center fluctuations are $(\Delta x_c, \Delta y_c, \Delta z_c) = (11.8, 1.25, 18.4)$ cm. It shows $\Delta z_c > \Delta x_c > \Delta y_c$ for bubble mass center fluctuations driven by gravity acceleration associated with slew motion.

The trend of the bubble mass center fluctuations, $\Delta z_c > \Delta x_c > \Delta y_c$, exactly reflects the values of the major driving forces of gravity gradient acceleration associated with slew motion in which it shows $g_z > g_x > g_y$ as that shown in *Figure 11*.

For a slew motion that operates with a range of 90° in 600 s, the component of jitter acceleration, based on equations (6), (8), (9), and (17), along the (x, y, z) directions acted on the fluid mass located at $(r, \theta, z) = (12$ cm,

$\pi/2$, 3 cm) is shown in *Figure 14*. This figure shows that the magnitude of gravity gradient acceleration is on the order of $10^{-5}\, g_o$.

Figure 15 shows the time evolution of the three-dimensional behavior of the interface oscillations driven by jitter acceleration associated with slew motion. In this figure, a time evolution of liquid–vapor interface profiles is shown at times t = 60.4, 258, 323, 354, 379, 403, 430, 528, 572, 628, 663, and 800 s. With reference to the characteristics of jitter acceleration associated with slew motion, shown in *Figure 14*, liquid is pushed toward the positive x- first and then to the negative x-directions, in combination with the negative z-direction. This makes the bubble to be pushed toward the negative x- first and then to the positive x-direction, together with the positive z-direction. These fairly complicated time-dependent variations of the dynamical forces exerted on the bubble create a series of bubble deformations as shown in *Figure 15*.

Time evolution of the locations of bubble mass centers of fluids inside the dewar container due to sloshing dynamics driven by jitter acceleration associated with slew motion based on *Figure 15* have been computed.

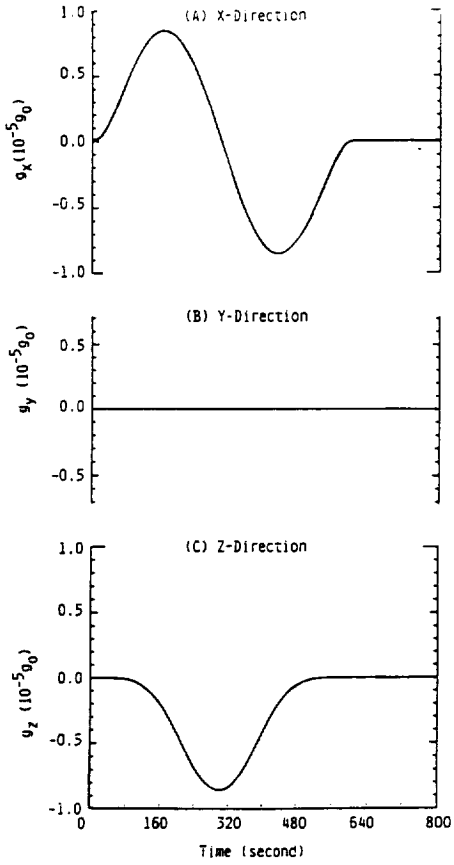

Figure 14. Time variation of AXAF-S spacecraft jitter acceleration associated with slew motion acting on fluid mass located at (r, θ, z) = (12 cm, $\pi/2$, 3 cm) for 90° slew motion in 600 s along the y'-axis and orbital period of 97.6 minutes along (A) the x-direction; (B) the y- direction; and (C) the z-direction.

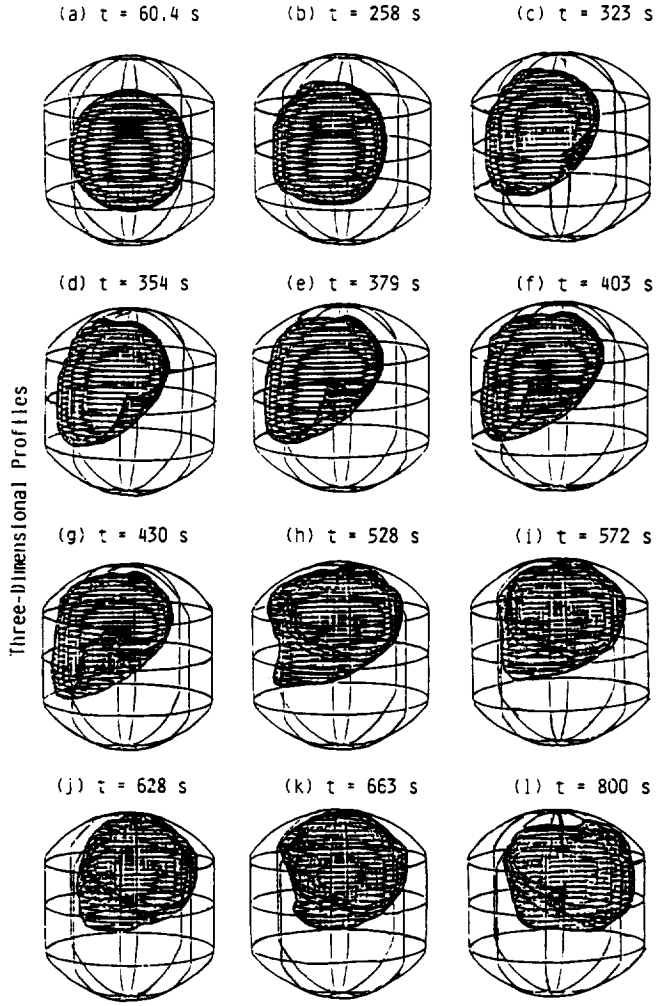

Figure 15. Time sequence evolution of AXAF-S spacecraft three-dimensional liquid–vapor interface oscillations for a dewar driven by jitter acceleration associated with slew motion in the y'-axis. 90° slew motion in 600 s is applied to the spacecraft operation.

The values of bubble mass center fluctuations are $(\Delta x_c, \Delta y_c, \Delta z_c)$ = (28.9, 0.44, 30.2) cm. It shows $\Delta z_c > \Delta x_c > \Delta y_c$ for bubble mass center fluctuations driven by jitter acceleration associated with slew motion. Behavior of bubble mass center fluctuations, shown in *Figure 15*, are the exact reflection of the behavior of jitter accelerations, shown in *Figure 14*.

Comparison between *Figures 14* and *15* illustrate some peculiar behavior of helium fluids with temperature below λ-point (2.17°K) in which helium demonstrates a number of remarkable properties of superfluidity, such as extremely low viscous and surface tension coefficients reacted to the disturbances driven by jitter acceleration associated with slew motion. It can be concluded as follows: (a) jitter acceleration associated with slew motion started at time $t = 0$. However bubble mass center fluctuations did not start to react to the driven force until t = 80 s for x_c and t = 160 s for z_c. In other words, the bubble configuration was perfectly spherical-shaped at 80 s after jitter acceleration associated with

slew motion was applied. (b) The x-component of jitter acceleration associated with slew motion was applied to the fluid element with a positive value from $t = 0$ to 300 s; a negative value from $t = 300$–600 s; and zero value after $t = 600$ s. However, westward movement of the bubble continued from $t = 80$–450 s and then switched to eastward movement to $t = 800$ s, which was 200 s after the acceleration vanished. Obviously there is a phase shift between the action of force and the reaction of motion. (c) The z-component jitter acceleration associated with slew motion was applied to the fluid element with a negative value from $t = 80$–500 s and the zero value after $t = 500$ s. However, the northward movement of the bubble started at $t = 160$ s, bounced back from the wall at $t = 530$ s, and then southward movement continued to $t = 800$ s, which was 300 s after the acceleration vanished. Obviously the motion continued for a long period of time even after the applied force vanished due to extremely low viscosity of helium II fluids. (d) An intensive oscillation of bubble with a deformation of irregular concave and convex shaped continued and sustained for several hundred seconds after the applied force vanished due to an extremely low surface tension coefficient for helium II fluids.

8. Discussion and conclusion

For different scientific missions, some experimental spacecrafts have to operate with various kinds of slew motion to perform their scientific experiments. In this study, both the GP-B and AXAF-S spacecrafts have been used as examples to show the mathematical modelling of bubble sloshing dynamics for cryogenic liquid helium in orbital spacecraft dewar containers. The instability of the liquid–vapor interface of the fluid systems can be induced by the presence of gravity gradient and/or jitter accelerations associated with spinning and/or slew motions of the spacecraft. These instabilities produced by sloshing dynamics can cause various problems in spacecraft control systems. Sometimes these sloshing dynamics can even deteriorate the quality of the normal operation of the spacecraft.

In this paper, a general mathematical model of sloshing dynamics of the dewar container partially filled with liquid driven by both a gravity gradient and jitter accelerations associated with spinning and/or slew motions were investigated. Two examples of the numerical simulation of sloshing dynamics driven by orbital accelerations, one with the GP-B for spinning motion and the other with the AXAF-S for slew motion, have been carried out. These examples demonstrate the variety of sloshing dynamics caused by the orbital accelerations associated with spinning and/or slew motions.

Acknowledgment

The authors appreciate the support received from the National Aeronautics and Space Administration through NASA Grants NAG8-129 and NAG8-938 and also NASA contracts NAS8-38609/Delivery Order Numbers 96 and 103.

References

1 Kamotani, Y., Prasad, A. and Ostrach, S. Thermal convection in an enclosure due to vibrations aboard a spacecraft. *AIAA J.* 1981, **19**, 511-516
2 Hung, R. J. and Shyu, K. L. Space-based cryogenic liquid hydrogen reorientation activated by low frequency impulsive reverse gravity thruster of geyser initiation. *Acta Astronautica* 1991, **25**, 709-719
3 Hung, R. J. Shyu, K. L. Constant reverse thrust activated reorientation of liquid hydrogen with geyser initiation. *J. Spacecraft Rockets* 1992, **29**, 279-285
4 Hung, R. J. and Shyu, K. L. Excitation of slosh waves associated with low frequency impulsive reverse gravity acceleration of geyser initiation. *Acta Astronautica* 1992, **26**, 425-433
5 Hung, R. J. and Shyu, K. L. Medium frequency impulsive thrust activated liquid hydrogen reorientation with geyser. *J. Propulsion and Power* 1992, **8**, 987-994
6 Hung, R. J., Lee, C. C. and Leslie, F. W. Effect of the baffle on the spacecraft fluid propellant viscous stress and moment fluctuations. *Trans. Jpn. Soc. Aeronaut. Space Sci.* 1993, **35**, 187-207
7 Hung, R. J., Lee, C. C. and Leslie, F. W. Effect of the baffle on the asymmetric gravity-jitter excited slosh waves and spacecraft moment and angular momentum fluctuations. *J. Aerospace Eng.* (United Kingdom) 1993, **207**, 105-120
8 Hung, R. J., Long, Y. T. and Pan, H. L. Sloshing dynamics induced angular momentum fluctuations driven by jitter accelerations associated with slew motion in microgravity. *Trans. Jpn. Soc. Aeronaut. Space Sci.* 1994a, **37**, 217-234
9 Hung, R. J., Pan, H. L. and Leslie, F. W. Gravity gradient or gravity jitter induced viscous stress and moment fluctuations in microgravity. *Fluid Dynam. Res.* 1994, **14**, 29-51
10 Hung, R. J., Pan, H. L. and Leslie, F. W. Fluid system angular momentum and moment fluctuations driven by gravity gradient or gravity jitter in microgravity. *J. Flight Sci. Space Res.* 1994, **18**, 195-202
11 Hung, R. J., Tsao, Y. D., Hong, B. B. and Leslie, F. W. Dynamical behavior of surface tension on rotating fluids in low and microgravity environments. *Int. J. Microgravity Res. Appl.* 1989, **11**, 81-95
12 Hung, R. J., Tsao, Y. D., Hong, B. B. and Leslie, F. W. Axisymmetric bubble profiles in a slowly rotating helium dewar under low and microgravity environments. *Acta Astronautica* 1989, **19**, 411-426
13 Hung, R. J., Tsao, Y. D., Hong, B. B. and Leslie, F. W. Bubble behaviors in a slowly rotating helium dewar in gravity Probe-B spacecraft experiment. *J. Spacecraft Rockets* 1989, **26**, 167-172
14 Hung, R. J., Lee, C. C. and Leslie, F. W. Effect of G-jitters on the stability of rotating bubble under microgravity environment. *Acta Astronautica* 1990, **21**, 309-321
15 Leslie, F. W. Measurements of rotating bubble shapes in a low gravity environment. *J. Fluid Mech.* 1985, **161**, 269-275
16 Mason, P., Collins, D., Petrac, D., Yang, L., Edeskuty, F., Schuch, A. and Williamson, K. The behavior of superfluid helium in zero gravity. *Proceedings 7th International Cryogenic Engineering Conferences*, Science and Technology Press, Surrey, England, pp. 230, 1978
17 Avduyevsky, V. S., ed. *Scientific Foundations of Space Manufacturing.* MIR, Moscow, 1984
18 Forward, R. L. Flattening space-time near the Earth. *Phys. Rev. D*, 1982, **26**, 735-744
19 Misner, C. W., Thorne, K. S. and Wheeler, J. A. *Gravitation.* W. H. Freeman Co., San Francisco, CA, 1973, pp. 1-1279
20 Van Sciver, S. W. *Helium Cryogenics.* Plenum Press, New York, 1986, pp. 429
21 Donnelly, R. J. *Quantized Vortices in Helium II.* Cambridge University Press, Cambridge, 1991
22 Wilks, J. *The Properties of Liquid and Solid Helium.* Clarendon Press, Oxford, UK, 1967

23 Hoare, F. E., Jackson, L. C. and Kurti, N. *Experimental Cryogenics: Liquid Helium II.* Butterworths, London, 1961

24 Hung, R. J., Pan, H. L. and Long, Y. T. Sloshing dynamics modulated cryogenic helium fluids driven by gravity or jitter accelerations associated with slew motion in microgravity. *Acta Mechanica Sinica* 1994, **10**, 367–381

25 Hung, R. J., Pan, H. L. and Long, Y. T. Peculiar behavior of helium II disturbances due to sloshing dynamics driven by jitter accelerations associated with slew motion in microgravity. *Cryogenics* 1994, **34**, 641–648

26 Hung, R. J. and Long, Y. T. Effect of baffle on slosh reaction forces in rotating liquid helium subjected to a lateral impulse in microgravity. *Cryogenics* 1995, **35**, in press

27 Wilkinson, D. T., Bender, P. I., Eardley, D. M., Gaisser, T. K., Hartle, J. B., Israel, M. H., Jones, L. W., Partridge, R. B., Schramm, D. N., Shapiro, I. I., Vessort, R. F. C. and Wagoner, R. V. Gravitation, cosmology and cosmic ray physics. *Phys. Today* 1986, **39**, 43–46

28 Stanford Relativity Gyroscope Experiment (NASA Gravity Probe-B). *Proceedings of Society of Photo-Optical Instrumentation Engineers* **619**, Society of Photo-Optical Instrumentation Engineers, Bellingham, WA, 1986, pp. 1–165

29 Hung, R. J. and Pan, H. L. Asymmetric slosh wave excitation in liquid–vapor interface under microgravity. *Acta Mechanica Sinica* 1993, **9**, 298–311

30 Hung, R. J. and Pan, H. L. Differences in gravity gradient and gravity jitter excited slosh waves in microgravity. *Trans. Jpn. Soc. Aeronaut. Space Sci.* 1993b, **36**, 153–169

31 Hung, R. J. and Pan, H. L. Fluid force activated spacecraft dynamics driven by gravity gradient and jitter accelerations. *J. Guidance Control Dynam.* 1995, **18**, in press

32 Hung, R. J. and Pan, H. L. Effect of baffle on sloshing modulated torques responded to orbital accelerations in microgravity. *J. Spacecraft Rockets* 1995, **32**, in press

33 Hung, R. J. and Pan, H. L. Rotational speed and wrapping of different size cryogenic helium bubbles around dewar well in microgravity. *Aeronaut. J.* 1995, in press

34 Hung, R. J., Lee, C. C. and Leslie, F. W. Slosh wave excitation in a partially filled rotating tank due to gravity jitters in a microgravity environment. *Acta Astronautica* 1991, **25**, 523–551

35 Hung, R. J., Lee, C. C. and Shyu, K. L. Reorientation of rotating fluid in microgravity environment with and without gravity jitters. *J. Spacecraft Rockets* 1991, **28**, 71–79

36 Hung, R. J., Lee, C. C. and Leslie, F. W. Spacecraft dynamical distribution of fluid stresses activated by gravity jitter induced slosh waves. *J. Guid. Control Dynam.* 1992, **15**, 817–824

37 Hung, R. J., Lee, C. C. and Leslie, F. W. Similarity rules in gravity jitter-related spacecraft liquid propellant slosh waves excitation. *J. Fluids Struct.* 1992, **6**, 493–522

38 Hung, R. J. and Leslie, F. W. Bubble shapes in a liquid-filled rotating container under low gravity. *J. Spacecraft Rockets* 1988, **25**, 70–74

39 Hung, R. J. and Shyu, K. L. Liquid hydrogen suction dip and slosh wave excitation during draining under normal and reduced gravity environment. *Trans. Jpn. Soc. Aeronaut. Space Sci.* 1994, **36**, 225–248

40 Hung, R. J. and Shyu, K. L. Liquid hydrogen shut-off geyser excitation induced by sloshing dynamics during draining in microgravity. *Aeronautical J.* 1994, **98**, 237–250

41 Landau, L. D. and Lifshitz, E. M. *Fluid Mechanics.* Pergamon Press, London, pp. 1–656, 1959

42 Hung, R. J., Shyu, K. L. and Lee, C. C. Medium frequency impulsive thrust excited slosh waves during propellant reorientation with geyser. *J. Propulsion Power* 1992, **8**, 778–785

43 Harlow, F. H. and Welch, F. E. Numerical calculation of time-dependent viscous incompressible flow fluid with free surface. *Phys. Fluids* 1965, **8**, 2182–2189

44 Spalding, S. D. A novel finite-difference formulation for differential expressions involving both first and second derivatives. *Int. J. Numer. Methods Eng.* 1972, **4**, 551–559

45 Patankev, S. V. and Spalding, S. D. A calculation procedure for heat, mass and momentum transfer in three dimensional parabolic flows. *Int. J. Heat Mass Transfer* 1972, **15**, 1787–1805

46 Patankar, S. V. *Numerical Heat Transfer and Fluid Flow.* Hemisphere-McGraw-Hill, New York, 1980